Eur Phys J C **33**, s01, s90–s106 (2004)
Digital Object Identifier (DOI) 10.1140/epjcd/s2004-03-1829-5

EPJ C direct
electronic only

Detector developments

Daniel Fournier

Laboratoire de l'Accélérateur Linéaire, Université Paris Sud, BP 34, 91898 Orsay Cedex, France

Received: 24 November 2003 / Accepted: 14 January 2004 /
Published Online: 8 April 2004 –

Abstract. Detector developments for elementary particle physics, with and without accelerators, are illustrated by a selection of experiments, presently under development or starting data taking

1 Introduction

Detector developments in the recent years are illustrated by a choice of experiments which led to significant progress in this field. Given the limited amount of time for the presentation, a choice among the extremely broad activity (see reports from parallel sessions) had to be made.

Despite the fact that gaseous detectors are so important in many experiments, but perhaps taking account that due to this, they are rather well known by the community, progress in this area will not be reported in any detail here. It should however be pointed out that large TPC's are presently being built, or are starting operation, for heavy ions collider physics (ALICE, STAR) [1] and that a TPC is also the choice tracker detector for a future linear collider experiment [2]. Beside TPCs, several impressive gaseous chamber systems are presently being built, in particular for muon instrumentation of LHC experiments. Particularly important in this context are MDTs, DTs and CSCs [3] for precision measurements, and RPCs and TGCs [4] for trigger purposes.

Coming back to the developments reported in some detail below, selected experiments have been clustered in two groups, first those not requiring accelerators, and then experiments with accelerators. In this last case, some generic R & D is also reported at the end.

Fig. 1. An aerial view of Virgo at Cascina, near Pisa

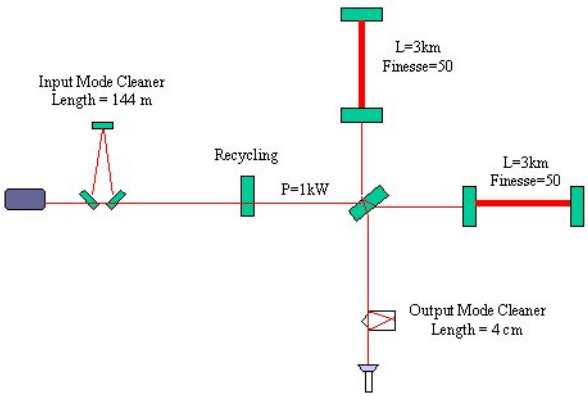

Fig. 2. Virgo optical scheme

2 Experiments without accelerators

2.1 LIGO and VIRGO

The detection of gravitational waves is an extremely challenging field, which entered a new era with the approach based on large scale interferometers. These devices are requiring in several areas an unprecedented level of sophistication, and represent a whole field of "detector development".

Send offprint requests to: Daniel Fournier: fournier@lal.in2p3.fr

2.1.1 VIRGO

It is particularly appropriate to talk about VIRGO, whose official date of completion coincides with the 2003 EPS Conference. The two Michelson arms of VIRGO (Figs. 1 and 2) are now part of the Pisa landscape.

Each arm is 3 km long with an optical length extended to $\sim$ 120 km by multiple reflexions between two mirrors in a Fabry-Perot configuration. The north arm was put under

Fig. 3. A Virgo mirror suspension tower (height about 10 m)

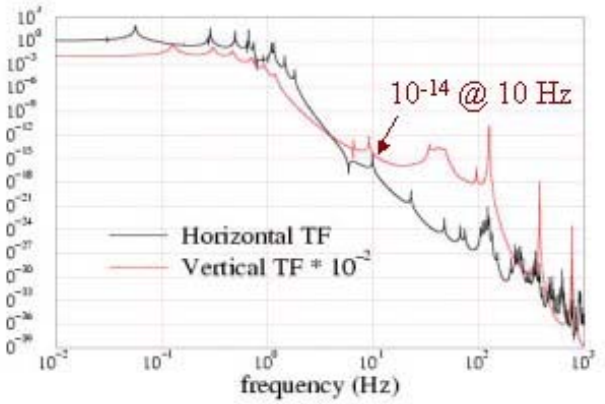

Fig. 4. Measured seismic rejection of a Virgo suspension

vacuum some weeks ago (10^{-9} mbar), to be followed soon after by the second one.

Over the last 12 months or so took place the commissioning of the Central Interferometer, a very important milestone of the project [5]. Schematically, during this phase, each Fabry-Perot arm is replaced by the end of arm mirror, about 6 meters away from the beam splitter. Running in this way allowed to tune and qualify several critical elements of the detector, in particular the suspension system, and the mirrors. The active suspension system (see Fig. 3) includes a 7 stage inverse pendulum. After suitable tuning the seismic rejection factor of 10^{14} at 10 Hz was met (Fig. 4). The high quality fused silica mirrors (Fig. 5) were also qualified, at the Virgo wave length of 1.06 μm. A higher power laser (20 Watts) was recently switched on. The full commissioning of Virgo will now start, with the

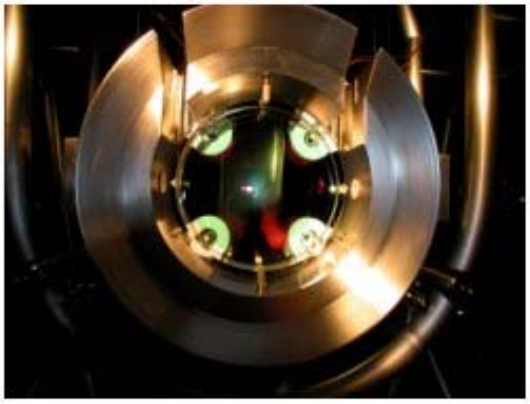

Fig. 5. Virgo beam splitter mirror in position (mirror diameter ∼30 cm)

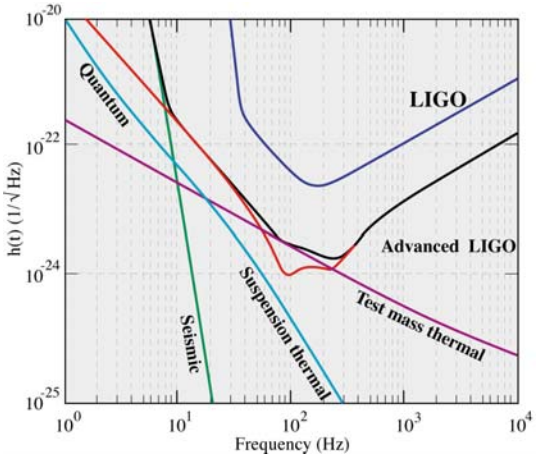

Fig. 6. Ligo sensitivity, nominal and upgraded

target of reaching the design sensitivity ($10^{-22}/\sqrt{Hz}$ or better between 30 Hz and 3 kHz) within ∼2 years.

2.1.2 LIGO

The LIGO experiment is somewhat ahead, with its two interferometers (Livingston and Hanford) already installed and their commissioning well advanced. Data taking (including coincidences) will start while the sensitivity is being continuously tuned and improved, with the aim of accumulating the equivalent of one year at 10^{-21} sensitivity by end of 2006 [6]. In parallel, a substantial upgrade plan was launched, with the aim of reaching a factor 10 improvement over the LIGO nominal sensitivity (see Fig. 6) by 2009.

The plan includes in particular improved suspensions, with an anti-seismic system along the lines taken by VIRGO, and improved mirrors (sapphire) capable of using the high power of a new 180 Watt laser.

2.2 Bolometers

For most detectors used in particle physics experiments, ionisation or light emission (scintillation or Cerenkov) are

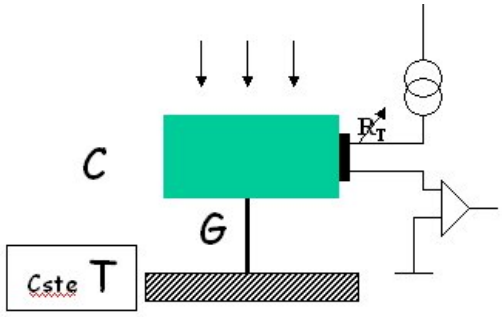

Fig. 7. Schematized bolometer

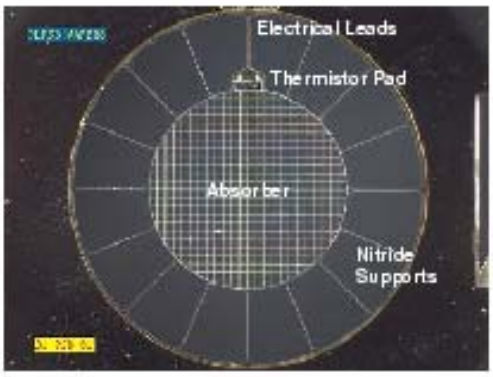

Fig. 8. Caltech spider web bolometer

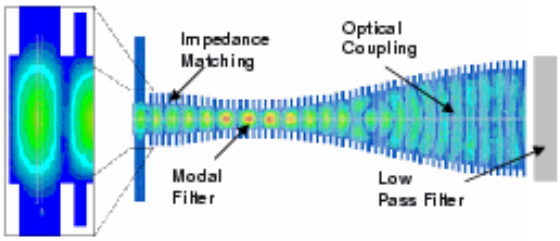

Fig. 9. Sketch of a coupling horn. The grid doublets are located at a maximum of the standing wave

the primary mechanisms on which the detection is based. In certain circumstances, namely at very low temperature, the transformation of part of the energy deposited by the particle(s) to be detected into heat can lead to extremely sensitive devices. This is the principle of modern bolometers, whose sensitivity was decupled when the temperature range of ∼100 mK and below became available. For practical reasons, bolometers are separated in the following in two main families:

- thin foils, or grids, dedicated to the absorption of electro-magnetic radiation in the few microns to mm wavelength range. They are the choice detectors for analysis of the Cosmic Microwave Background.
- massive crystals for detecting recoils from dark matter collisions.

2.2.1 General features of bolometers

Schematically (see Fig. 7) a bolometer consists of an absorbing crystal, of heat capacity C (for an insulator C is proportional to T^3 while the free electrons specific heat goes like T). The absorber is connected to a constant temperature reservoir at temperature T, with a link of thermal conductance G.^{3}He/^{4}He dilution refrigerators [7] are the choice technology below 200 mK.

The sensor, glued to the crystal is primarily a temperature dependent resistor R_T. Neutron Transmutation Doped germanium crystals are widely used. Super- conducting "transition edge" foils are even more sensitive, but in general operate in a more reduced temperature range. The main contributions to the noise equivalent power at the amplifier input are dominated by [8]:

- the Johnson noise in R_T $(NEP)^2=4kTR_T\delta F$
- the heat fluctuations along G $(NEP)^2=4kT^2G$

An important system parameter is the time constant $\tau = C/G$.

2.2.2 Bolometers for CMB detection

An elegant solution for these bolometers is based on the work pioneered by Caltech-JPL [9]. Using Si wafer technology, a thin spider web is obtained from a Si nitride layer (see Fig. 8), after that "all the rest" has been etched away.

Typical parameters of such grids are a diameter of 2.5 mm, a thickness of 4 μm, covered by a few nm of metal, giving a heat capacity below 1pJ/K at 100 mK. In comparison, the CMB absorbed power in a frequency range of $\sim 10\%$ around 200 GHz is about 0.01 pJ in ∼10ms. With a NTD-Ge thermistor,the noise power can be better than $10^{-17}\mathrm{W}/\sqrt{Hz}$.

Taking advantage of the possibility to metallize one direction or the other of the grid, the polarisation of the CMB can be measured by difference in an elegant way. This was recently demonstrated in the flight of the Boomerang balloon [10].

All these techniques will be implemented in the High Frequency Instrument of the Planck mission, to be launched by ESA in 2007 [11]. A view of a coupling horn is shown in Fig. 9.

Beyond these important ongoing realisations, developments are being conducted in order to realize arrays of bolometers (including the sensor) which would improve the overall efficiency per unit area in the focal plane.

2.2.3 Massive bolometers

The sensitivity of experimental set-ups dedicated to the direct search of non-baryonic dark matter by detection of nuclear recoils goes directly with the instrumented mass, calling for a larger and larger number of massive bolo-

metric crystals (typical examples are 320g Ge crystals). Even in well shielded underground laboratories and using low radioactivity materials, Compton electron recoils from residual gamma radioactivity remain an important background in this search. In order to reject these backgrounds some identification of the nature of the recoil, nuclear or electronic, is necessary. This can be provided by a combined detection of heat and scintillation, or heat and ionisation, taking advantage of the fact that for a given bolometric signal, nuclear recoils produce less ionisation, and to a lesser extend, less scintillation than electromagnetic deposits. Another approach is to combine light and ionisation detection, like the ZEPLIN group [12] is doing with liquid Xenon as a detector.

The combined detection of heat and ionisation is illustrated below, taking as example the Edelweiss experiment [13]. A similar approach is used by CDMS [14], while CRESST and ROSEBUD combine heat and scintillation [15]. In order to be sensitive to ionisation, the extra-pure Germanium crystals cut in a cylinder with axis along the $< 100 >$ direction have their opposite faces ($\emptyset \sim 70$ mm) metallized with 100 nm read-out electrodes. The crystals are operated in the 20 mK range, and the heat signal is read-out using Ge-NTDs. The detection threshold energy is about 5keV and the noise about 1 keV. A polarisation voltage as low as 3V is enough to drift ionisation (without creating parasitic heat load) over 1cm in less than 400 ns, thanks to the high mobility at low temperature in ultra-pure crystals. The energy resolution of the ionisation measurement is also of order 1 keV.

The response of the detector to nuclear recoils and electron deposits is calibrated using ^{60}Co gamma sources and ^{252}Cf neutron and gamma sources. As shown in Fig. 10, the electromagnetic and nuclear recoils are well separated.

Based on the absence of events in the nuclear recoil band, Edelweiss gave one of the best limits on non-baryonic dark matter search. A further step will be made,bringing sensitivity down to 10^{-8} pb, when the 120 detectors representing 35 kg active, will be operational. This level of sensitivity is within the range predicted by some super-symmetric models. In parallel with this effort of enlarging the detector, R & D is being pursued regarding the use of temperature sensors even more sensitive than Ge-NTDs, like super conducting transition edge detectors.

2.3 High energy photons from space

Being unperturbed by magnetic fields, high energy gamma rays from space provide a unique capability, in the high energy domain, for source identification. The range from 20 MeV to 300 GeV, not easily accessible to ground based experiments (Cerenkov signals from atmospheric absorption are too faint), is well matched to satellite experiments.

This domain was pioneered by EGRET [16]. A new generation detector, GLAST [17], is presently under construction after a careful optimisation. The main part of the mission is the Large Angle Telescope, complemented by gamma ray detectors in the 20 keV to 20 MeV range.

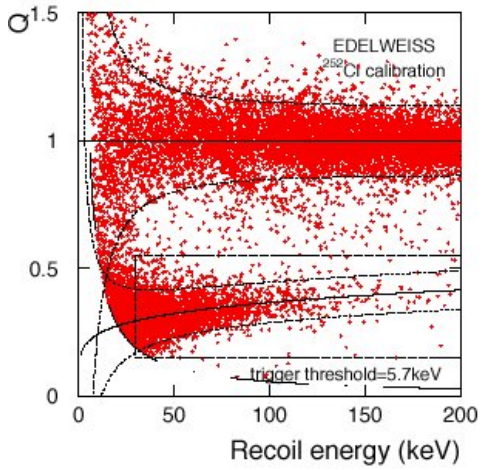

Fig. 10. Ionisation to heat ratio as observed with a Cf source in Edelweiss. The electrons (ratio∼1) and recoils from neutron collisions are clearly separated

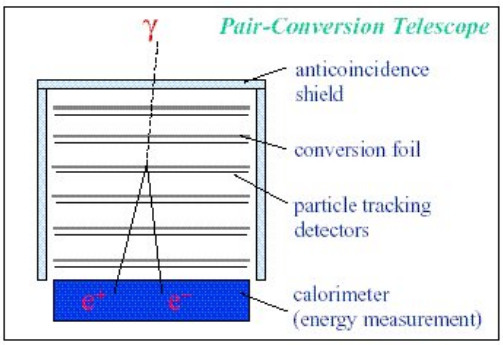

Fig. 11. Sketch of the GLAST-LAT detector layout

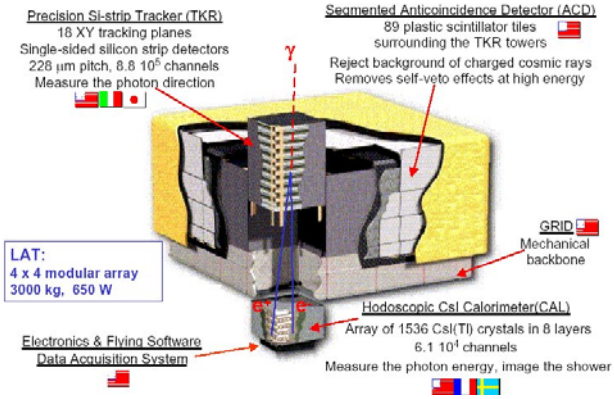

Fig. 12. Artist view of GLAST

2.3.1 Principle of the LAT

The detector is arranged as 4x4 adjacent submodules, with a total transverse size of 1.7 x 1.7 m^2 and 87.5 cm height. The direction of high energy photons is measured from their conversion products in the Large Area Telescope made of semi-conductor strip sensors interleaved with thin converter foils (see Fig. 11).

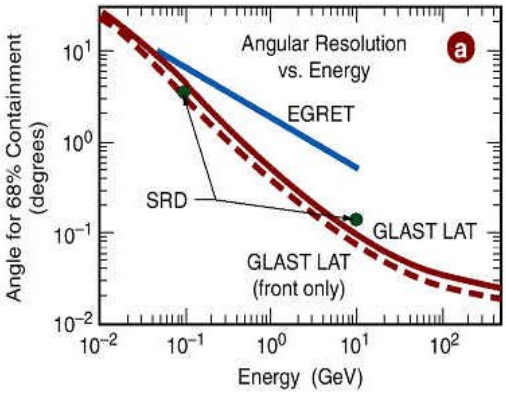

Fig. 13. Angular resolution of GLAST (simulation)

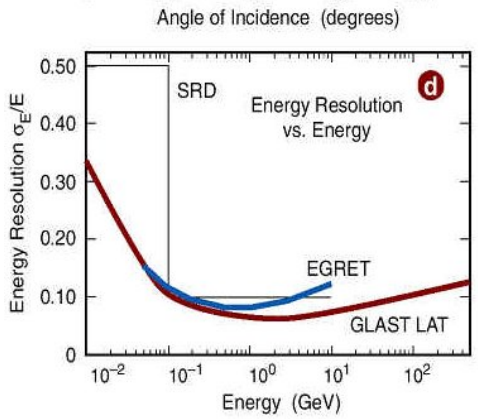

Fig. 14. Energy resolution of GLAST (simulation)

The Si-strip detectors have a pitch of 228 microns, and a length of 4 x 9 cm obtained by wire bonding 4 sensors on a ladder. The total number of channels is 8.8 10^5. Fabrication used for the first time, on large scale, 6" high resistivity wafers. Readout is ac coupled to p^+ strips on n-type Silicon. The energy of the converted electrons (and further constraint on the direction) is obtained from a calorimetric energy measurement. The choice was made of using CsI crystals, in an XY geometry, with a total thickness at normal incidence of $8.5X_0$ (see Fig. 12). Such a total thickness is by far insufficient to contain photon showers at the high end of the spectrum, but was dictated by the strong constraint of a maximum weight of 3000 kg. Besides the weight, another hard limit in a satellite is the power dissipation. With a total budget of 650 W, the Si-strips use only 210 W and the calorimeter only 90 W. Another important element of the detector is a segmented anticoincidence array, made out of scintillator tiles. A rejection factor of 10^5 against charged particles is required.

2.3.2 Detector qualification

The energy and the direction resolution of the detector were studied with detailed simulations and test beam data recorded at SLAC [18]. The optimum found for direction measurement features 18 X-Y detection planes. The first 12 are associated to 3% X_0 W converter, the next 4 to 18% X_0 W converters, and the last 2 have no converters.

As an illustrative figure, the angular resolution (see Fig. 13) at 10 GeV is 0.15 degrees, about 10 times better than one can achieve with a finely segmented calorimeter alone.

Thanks to the several samplings provided by the XY geometry of the crystals, the group has shown that the detector can provide a relative energy resolution of 15% (5%) up to the end of the accessible spectrum for photons at 90 degrees (below 60 degrees) incidence (see Fig. 14).

2.3.3 Next steps

The qualification of the detector elements is presently ongoing. It includes severe vibration tests, an exposure to ion beams to check for SEE and cosmic tests. Launching of the satellite by NASA is planned for fall 2006.

2.4 High energy neutrinos from space

The long term aim of experiments (or R & D projects) like Amanda [19], Antares [20] or Nestor [21] is to instrument 1 km^3 of water in order to be sensitive, with enough pointing accuracy, to high energy neutrinos from space. In both cases the detection is based on Cerenkov light produced in water (or ice) by secondary muons from neutrino interactions in earth.

2.4.1 Deployment in water

Antares and Nestor are taking up the challenge of deploying their detectors in sea water. This is one of the first main challenges of their first phase covering about 0.03 km^3. Compared to ice (Amanda), water offers a longer scattering length (∼300 m against ∼20 m) due to the absence of micro bubbles, and the possibility to go to higher depth (down to 4000 m in the case of the Nestor site). On the other hand, operating in water brings several problems:

- ^{40}K radioactive isotopes in salt water produce a ∼50 kHz counting rate in a 10" photomultiplier.
- alive micro-organisms produce bioluminescent "bursts" during which the counting rate can reach several 100 kHz.
- water is a moving medium imposing continuous survey of active elements (to an accuracy of 20 cm or so).

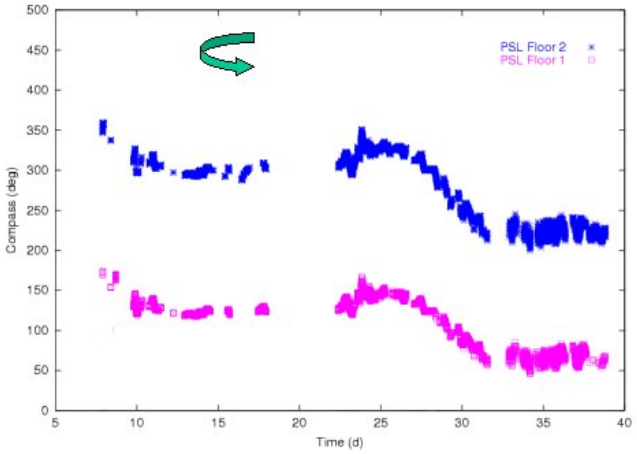

Fig. 15. Antares compass angle as a function of time

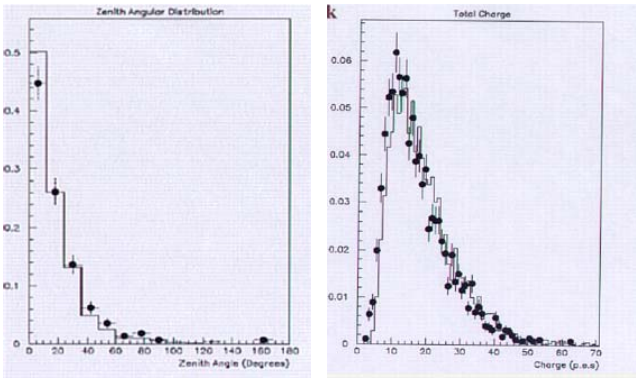

Fig. 16. Zenith and energy distribution in a Nestor tower

2.4.2 Results from recent tests

The first phase of Antares includes:

- 12 lines of 25 x 3 optical modules (10"PMT)
- local self-triggering, digitisation and time stamp
- an electro-optical cable (48 optical fibers, 4400 Vac) from shore.
  A first line was deployed in spring 2003, leading to the following observations:
- the ^{40}K rate of 50 kHz is confirmed, but there is somewhat more bioactivity (up to 30% of the time) than in a previous test. This could be a seasonal effect.
- the variation with time of the twist angle ("compass") at two heights on a given line is illustrated in Fig. 15, demonstrating the necessity of continuous survey.

In their new test the Nestor group was quite successful. A complete floor, diameter 32 m, with 12 optical modules (half of them oriented "up") was deployed early in 2003, and readout with the 30 km electro-optical cable to shore. Nestor uses 15"PMT (144 in a tower), which showed the expected ∼70 kHz ^{40}K background. The bioluminescent background is low, giving less than 1% dead time. Some muon data (from above..) were recorded, asking for a 4-fold coincidence with a single PMT threshold of 1/4 photo electron. In these conditions the rate is low (few Hz). Figure 16 shows the pulse height and zenith distribution (calculated with the time of arrival of various signals) obtained in this run.

Fig. 17. Icarus T600 detector during installation

2.4.3 Next steps

While both Antares and Nestor tests were extremely useful to the collaborations, several important R&Ds remain necessary before entering the 1 km^3 phase. The developments include improved reliability of immersed equipment, means of access and repairs, high power, high rate electro-optical cables,....

2.5 ICARUS

While this is not a new development, it is appropriate here to mention the important forward step recently achieved by the ICARUS collaboration which operated successfully the T600 prototype with cosmics [22].

The ICARUS T600 prototype consists of two containers in a single cryostat. Each container is a liquid argon TPC with a gap of 2 x 1.5 m operated with a 75 kV polarisation voltage. The detector length is 20 m and its height 4 m. In each detection plane 3 wire planes at 45° of each other (27000 channels of electronics) give a 2D picture as a function of time, thus providing a full 3-D imaging.

The ionisation electron life time was measured above 1 ms, adequate for drift lengths up to 1.5 m. Large (8") VUV photomultipliers are used to self-trigger the detector using the scintillation light of liquid argon (peak wavelength 130 nm, average light yield ∼ 20 eV per photon).

Figure 17 shows the T600 detector during installation, and Fig. 18 shows a cosmic muon with an EM shower.

Next steps in the ICARUS project include moving the T600 to the CNGS neutrino beam in the Gran Sasso laboratory and adding two 1200 tons modules to reach 3000 tons. Operating and storing such large liquid argon masses, and beyond, in an underground laboratory, raise safety issues on which the groups involved are actively working.

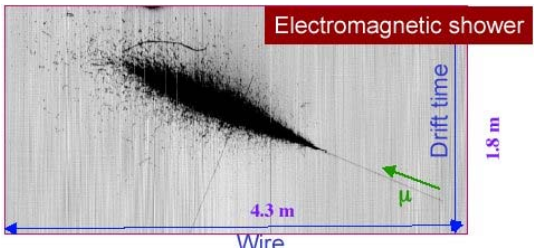

Fig. 18. EM shower along a cosmic muon, recorded by ICARUS

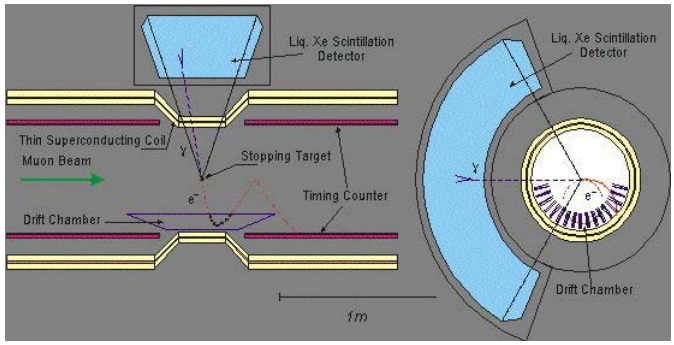

Fig. 19. The MEG experiment layout

3 Experiments with accelerators

3.1 Rare decays

Rare decay experiments often led in the past to interesting detector developments, motivated by the need of selective detection in a high rate environment and precision measurement. An interesting example, currently under development, is the MEG experiment dedicated to the challenging search of the lepton number violating decay $\mu \to e\gamma$.

3.1.1 Motivations and layout

Searches for $\mu \to e\gamma$ decays were negative up to now with an upper limit of 10^{-11} branching ratio [23]. There are however indications that this decay should happen – one day – at measurable levels. Some quantitative estimates based on the observation of atmospheric neutrino oscillations point to a decay branching ratio of 10^{-14} or larger [24]. Several Supersymmetric models give a branching ratio between 10^{-11} and 10^{-13} [25].

The MEG Collaboration is taking up the challenge of probing this decay at the 10^{-13} level. The necessary stopping muon rate of $\sim 10^8$/s is available at the PSI (Villingen) site, where the experiment is under construction. In order to cope with this rate, and to have the required rejection of background (in particular radiative beta decays), the best possible photon calorimeter (in terms of speed, energy and position resolution) in the 50 MeV range is required.

The collaboration has chosen a liquid Xenon calorimeter, presently under construction after a vigorous development programme. A light-weight precise tracking for the secondary electron is also necessary. A sketch of the experimental arrangement [26] is shown in Fig. 19.

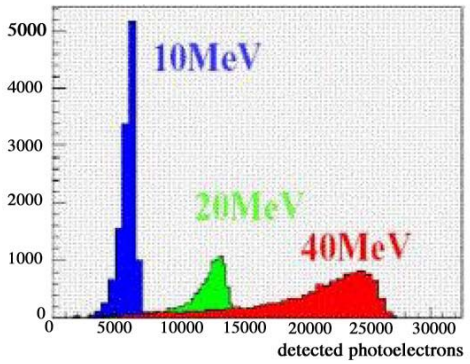

Fig. 20. Energy spectra of quasi-mono energetic photons in the MEG prototype

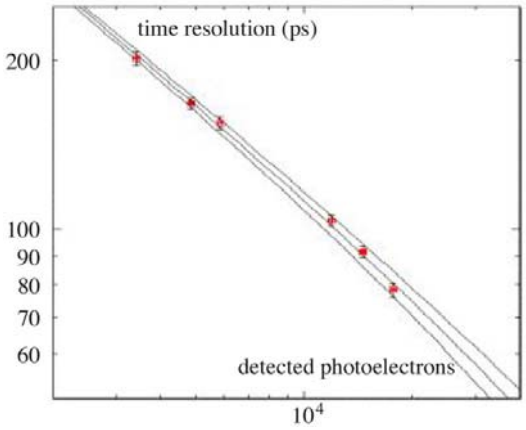

Fig. 21. Time resolution for photons in the MEG prototype calorimeter

3.1.2 The Xenon calorimeter

The detection uses the scintillation light produced by Xenon. As several developments and small scale detectors showed in the past, liquid Xenon is an excellent scintillator [27] with high photon yield (∼24 eV/photon), and fast decay time (2 time constants of 4.5 and 22 ns). The wavelength (175 nm) requires VUV windows. Before launching the construction of the final calorimeter (800 l Xenon, the largest quantity used so far for physics, 800 PMTs), a number of studies and developments were carried out with prototypes, the last one of 70 l active, viewed by 150 PMTs. The most significant results of this programme [28] are reported below.

Regarding the liquid purity, the absorption of scintillation light by water, and to a lesser extend by oxygen was found to be a potential problem. Absorption lengths of 1 m or larger were found to require less than 1 ppm of oxygen, and less than 100 ppb of water, and the necessary filtering system was developed. Special PMTs, compatible with operation immersed in liquid Xenon were also devel-

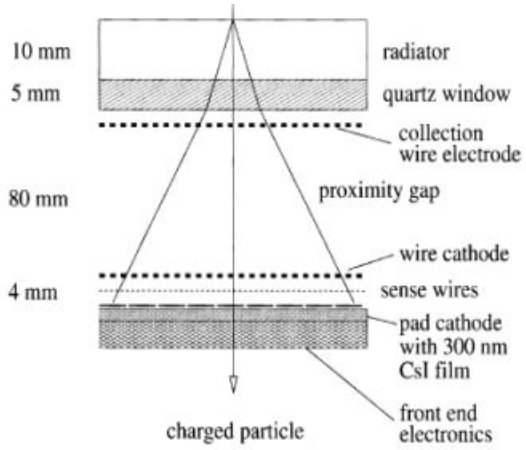

Fig. 22. Sketch of a RICH equipped with CsI photocathodes

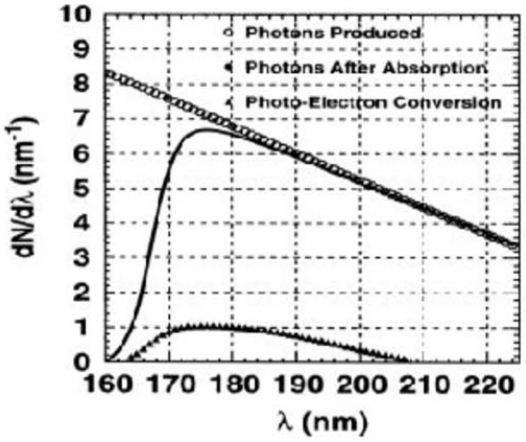

Fig. 23. Photon spectrum in CsI RICH up to conversion

oped. It was also shown that separating the active volume into optically isolated cells by thin reflective layers will improve the calorimeter performance.

Finally the performance of the large prototype was assessed with a photon beam obtained by laser backscattering on an electron beam at TERAS in Japan. The energy resolution (2% at 40 MeV) and time resolution (70 ps at 50 MeV), shown in Fig. 20 and Fig. 21, are well within the severe requirements of the experiment.

3.1.3 Next steps

The design of the final calorimeter is now being completed. Its construction will then proceed. The construction of the rest of the equipment being well advanced, the experiment plans to start data taking in 2005.

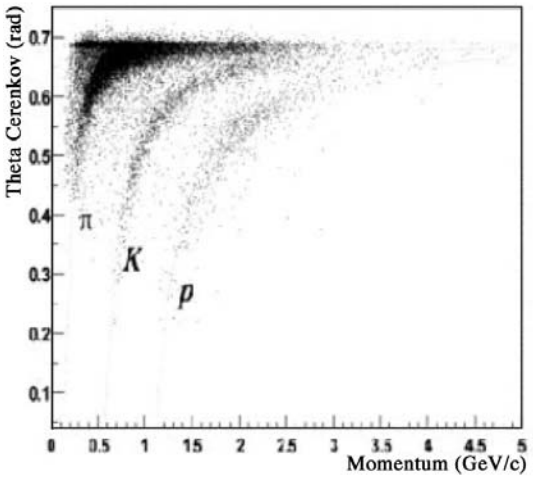

Fig. 24. Particle ID at STAR with a CsI Rich

3.2 Particle identification

Particle identification can be interpreted in several ways, going from a specific detector, like a threshold Cerenkov counter giving a yes/no signal for a pion/kaon traversing it, to sophisticated reconstruction in complex events used to identify a short lifetime particle, like a D or B meson. In the following only two examples are taken, as illustration of this broad field.

3.2.1 Use of CsI photocathodes in RICH detectors

At the expense of difficult constraints on detector size or geometry, Ring Imaging Cerenkov counters were included in several colliding beam detectors like DELPHI at LEP. The use of Cesium Iodide as a covering layer of MWPCs dedicated to the conversion and detection of Cerenkov photons had the promise of a gain on space, and speed of response.

The development of such chambers was carried out in the framework of the RD26 project. In the last few years, detectors of large size were equipped with such chambers. Examples include COMPASS, HADES, STAR at RHIC and ALICE at the LHC [29]. A sketch of the principle of a RICH system working in this way is shown in Fig. 22. Different effects affecting the useful photon spectrum are shown in Fig. 23. The CsI film is typically 300 nm thick; this layer is extremely sensitive to water absorption: from cathode coating to data taking, the layer should never be in contact with open air...

The ALICE 1 m^2 prototype installed and used for some time in STAR is discussed below. The Cerenkov radiating medium is a 1 cm thick C_6F_{14} liquid radiator closed by a UV-grade fused silica window. The distance from radiator to photo-detector is 80 mm, optimised to let the rings expand for better pattern recognition. The cathode pads covered by CsI have a size of 8 x 8 mm. Figure 24 which shows STAR data taken at RHIC illustrates the potential of the detector in a high density environment. Following these encouraging results, the ALICE collaboration is now engaged in the construction of its final CsI RICH (12 m^2 active).

3.2.2 On-line B tagging at the Tevatron

The physics of B mesons is an important part of the ongoing Tevatron run II. In order to be able to study as many as possible of the numerous B meson decay modes, a trigger acting at low level was developed for CDF II [30]. The trigger is based on the on-line recognition of displaced secondary vertices (cutting on the tracks impact parameter) and is applied to any event which has at least two charged tracks with a $P_\perp$ of 2 GeV/c or more. This condition is part of the LVL1 menu whose maximum overall rate is 45 kHz.

3.2.2.1 Hardware implementation

The CDF SVX II vertex detector is formed of 5 concentric "cylinders"(maximum radius 10.6 cm, minimum radius 2.5 cm, length 90 cm) instrumented with Silicon detectors with strips running parallel to the beam axis. The geometry is such that data can be treated as coming from 12 independent sectors in azimuth. Inefficiencies due to tracks at the sector boundaries remain at the few % level. In the present scheme only the 4 outer layers out of 5 are used (there is in addition another layer at smaller radius not used in the trigger).

The information fed to the processing electronics consists of:

- 1 "point" at an intermediate radius of the Central Tracker, with its azimuth and curvature, for all track candidates found at LVL1 in a given sector of the CT.
- azimuthal pattern of hits in all 4 layers of the vertex detector for this sector. At this level Si microstrips are grouped into an equivalent pitch of 250 μm in order to limit the number of inputs.

In a first step, the processing electronics (based on Associative Memories) compares this information to a set of 32000 coded masks representing "valid tracks" and finds all track candidates at the vertex detector level.

In a second step the precise fit of the tracks in r-phi is made, with the impact parameter as one of the outputs. Displaced vertices are found by selecting those tracks above a certain impact parameter threshold.

3.2.2.2 Performances

The SVT trigger requires an average processing time of 25 μs and its efficiency is on average 80%.

As an illustration of the performance of this system [31], Fig. 25 shows the distribution of reconstructed impact parameters. The average resolution of 48 μm receives about equal contributions from the measurement accuracy (35 μm) and the beam precision (33 μm). This last number underlines that such a system can only give its best performances with a well centred, narrow and stable beam crossing in the transverse plane, which the Tevatron is now able to deliver.

A typical mode of operation of the displaced vertex trigger is to retain events with at least one track displaced by more than 120 μm. In these conditions the rate of retained events is 5 Hz (among $\sim$ 350 Hz total at this trigger level) demonstrating, together with the efficiency, the excellent performance of the system.

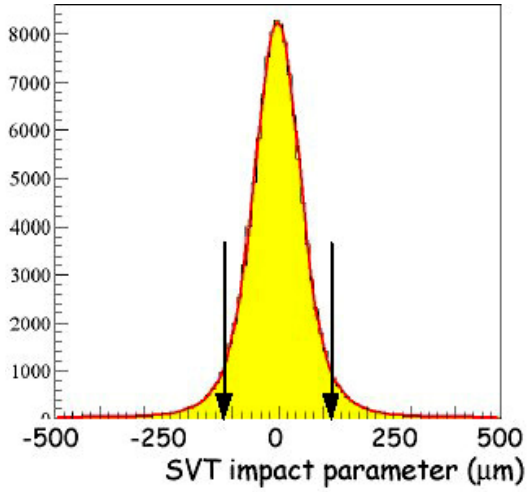

Fig. 25. Distribution of impact parameters at the output of the CDF vertex trigger. Arrows indicate the selection cut

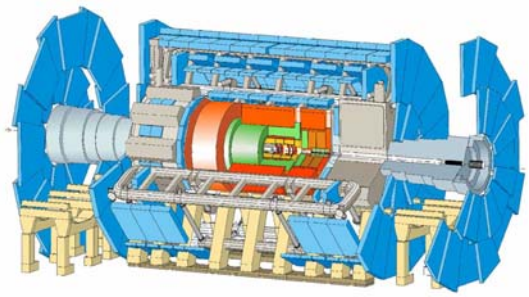

Fig. 26. Atlas detector layout

Displaced vertices will be part of the High Level Triggers of the LHC experiments as well (see below). Their spirit is however somewhat different, both in the Physics to be retained, and in the way they are implemented.

3.3 The ATLAS and CMS experiments at the LHC

The Aachen workshop, in October 1990, is considered by many as the start of the LHC experimental programme. During the 13 years which have passed since then, a first phase was a detailed optimisation of the experiments, combining the requirements for physics, with the constraints posed by detector developments and integration. This phase culminated with the Technical Design Reports submitted as of early 1996, in which the layout of the experiments, optimised for the normal high luminosity of $10^{34}\mathrm{cm}^{-2}\mathrm{s}^{-1}$ (see Fig. 26 and figure 27) was frozen.

The second phase was to launch the detector construction, which is now well advanced. It is not possible here to report on all these aspects, many of which represent major steps in "detector development". A few examples of magnets, muon detectors, calorimeters, and tracking devices, are taken in each experiment, going from outside to

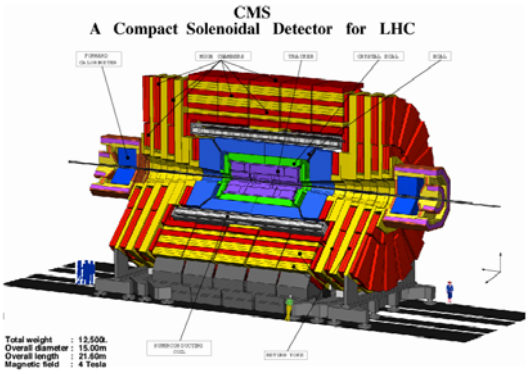

Fig. 27. CMS detector layout

Fig. 28. CMS solenoid: winding of first longitudinal section

inside, illustrated by photos of construction, and some key performance parameters.

3.3.1 the CMS solenoid

The CMS solenoid [32] will surpass in diameter (6.5 m), length (12.5 m), and magnetic field (4 T) all solenoids built so far. The stored energy (2.6 GJ) is going to be a world record. The constraints posed by these requirements led to a complex coil structure: it is mechanically split in 5 longitudinal sections (in a single cryostat), and each section has 4 layers of conductor. The super-conducting cable is embedded in pure aluminium, with a further reinforcement of Al alloy. The nominal operating current is 20 kA; the total cold mass is 220 t. Figure 28 shows the first longitudinal section CB-2 during winding of the conductor inside its mandrel. The complete coil will be tested in a surface hall (mid 2005) before being lowered in the CMS pit.

3.3.2 ATLAS magnets

ATLAS has chosen a toroidal structure-barrel and two end-caps-for its muon spectrometer. A small-compared to CMS-solenoid houses the tracking system. Particularly challenging in this system is the barrel toroid [33], made out of 8 race-track coils assembled by a warm structure. Each coil is 25 m long, 5 m wide and features a cold mass of about 45 t. The nominal operating current is 20 kA. The field integral at 90 degrees is about 4 Tm. The stored

Fig. 29. Atlas barrel coil casing

Fig. 30. Atlas barrel coil pancake

energy (barrel and two end caps) is about 1.6 GJ. Figure 29 shows a coil casing where two coil pancakes (Fig. 30) will be located. Each coil will be cold tested in a surface hall starting end of 2003.

3.3.3 ATLAS muon alignment

The somewhat smaller bending power of the Atlas toroid, in air, compared to the instrumented iron flux return of the CMS solenoid, calls for higher precision measurements of muon tracks, and thus for high precision "alignment" of muon detectors. A typical figure is a systematic precision of 30 μm over distances of 5 to 10 m. The selected system uses coded masks, lenses, and scanning cameras. A prototype was operated successfully in recent beam tests at CERN, and gave an accuracy for movements transverse to the light beam of about 15 μm. A sketch of the various elements of a barrel octant is shown in Fig. 31. In total ATLAS will be equipped with about 10000 position sensors [34].

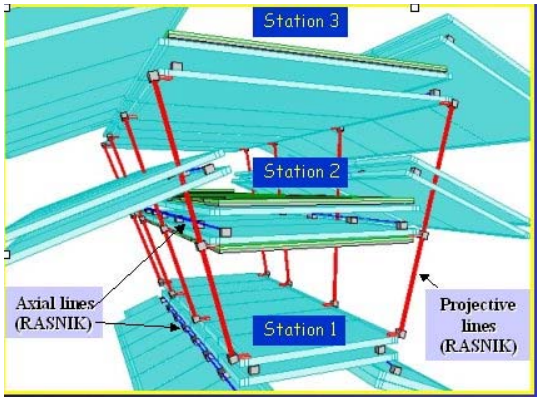

Fig. 31. Sketch of the ATLAS muon alignment system

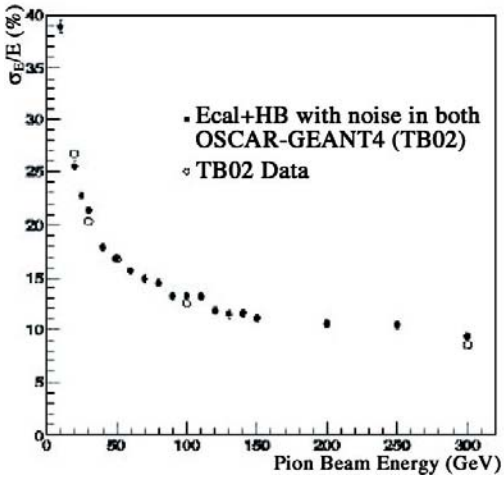

Fig. 32. Performance of the jet calorimeter system of CMS for single pions

3.3.4 CMS hadronic calorimetry

Jet energies are measured using both the electromagnetic calorimeter, where the neutral component of the jets, and the first part of the hadronic cascade are absorbed, and the hadronic calorimeter which absorbs the bulk of the hadronic part. The hadronic calorimeter of CMS [35] uses 5 cm thick brass plates as absorber, interleaved with 1 cm thick scintillator tiles readout by wave length shifting fibers (granularity $\delta\eta$ x $\delta\phi = 0.087$ x 0.087). In turn, WLS fibers are spliced to clear fibers allowing to bring signals in the back of the calorimeter and to regroup tiles belonging to the same tower. Hybrid Photo Detectors (gain $\sim$ 2000) are used to make the light to electronic signal conversion.

For $|\eta|$ <0.4 a tail catcher follows the coil in order to bring the total calorimeter thickness up to the last active layer from 8 to 12 interaction lengths.

The CMS group has tested in 2002 a combination of a movable 7 x 7 matrix of $PbWO_4$ crystals (see below), in front of two modules of the barrel hadronic calorimeter (2 x 20 degrees of azimuth, 4 m long). The setup was complemented by an aluminium slab representing the coil, and a section of the tail catcher. The energy resolution obtained for pions between 20 and 300 GeV/c is shown in Fig. 32. It can be fitted by $\Delta(E)/E = 120\%/\sqrt{E} + 4\%$ and is well reproduced by a Geant4 simulation [36] (no weighting scheme is used at this stage). The construction of the barrel hadronic calorimeter is now essentially complete as illustrated by Fig. 33.

Fig. 33. The hadronic barrel calorimeter of CMS in the assembly hall

3.3.5 CMS EM calorimeter

After a long and thorough development period, CMS has chosen $PbWO_4$ crystals for its electromagnetic calorimeter [37], barrel (inner radius=1.3 m) and end-caps (front face at $|Z|$=3.2 m).

3.3.5.1 The $PbW0_4$ crystals

The production of crystals is taking place in Russia. Important progresses were made in the growing of ingots which are now 85 mm in diameter and allow obtaining from one piece either 4 barrel crystals (transverse size 21.8 x 21.8 mm corresponding to a granularity of 0.0175 x 0.0175) or two end cap crystals(transverse size 29.6 x 29.6 mm). The light to electronic signal conversion is made with two Avalanche Photo Diodes glued on the back face of each crystal. The internal gain of APDs is about 50. In the end-caps, Vacuum Photo Triodes were preferred, for better radiation resistance.

At the time of the Conference about 1/3 of the barrel crystals (62000 in total) and more than half of the APDs were delivered and being submitted to strict QC. One of the criteria is that each crystal+APDs give more than 6 photo-electrons per MeV. The front-end electronics will finally be made with CMOS Deep Sub Micron (0.25 μm) ASICS, after recent successful tests. The electronics noise per crystal is expected to be about 30 MeV (8000 electrons) at start-up, with some increase at high luminosity due to leakage current in APDs induced by irradiation. The dynamic range of $\sim$16 bits is covered using a 3-gain system (in the ratio 1: 6: 12). Digitisation, and local sums

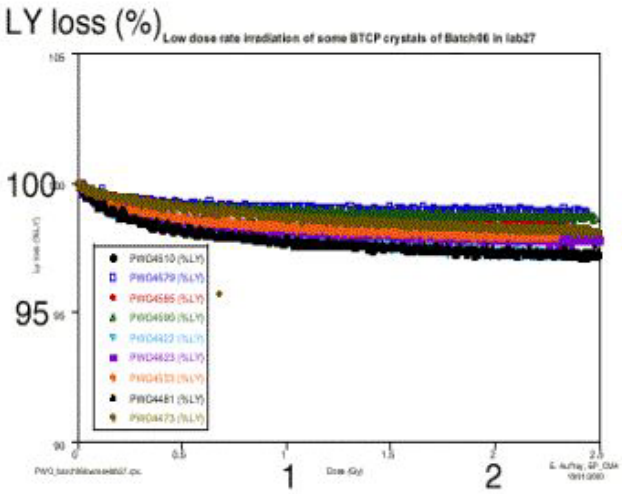

Fig. 34. Light loss observed in electron test beam with several crystals

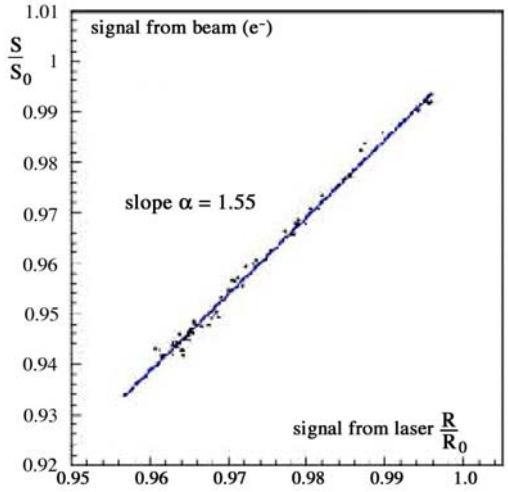

Fig. 35. Correlation of losses as seen by laser pulses and beam particles

for first level trigger are made on detector. Transmission of complete data for readout is made upon first level trigger request. A Si preshower is installed in front of the end caps.

3.3.5.2 Constant term and calibration

The target constant term of the CMS electromagnetic calorimeter, 0.5%, calls for strict control of several systematic effects. As a first example, the temperature dependence of about -4% per degree (shared about equally between crystals and APDs) imposes a control of cooling and thermal isolation to 0.1 degrees or better.

An other potential source of systematic uncertainty is related to the effect of radiations on the crystals themselves. Several tests have shown that the light yield of the crystals drops by a few percents after even a modest dose

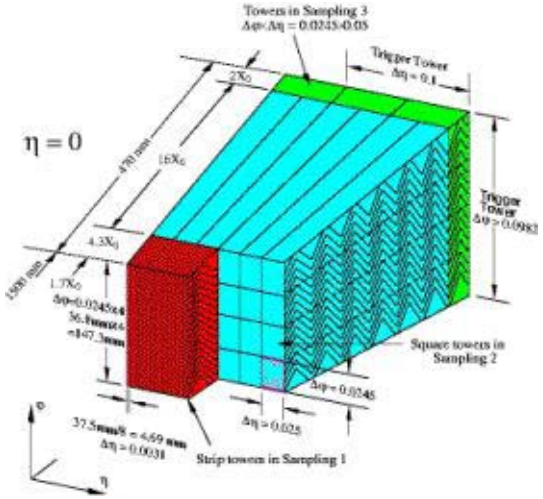

Fig. 36. Sketch of the "accordion geometry" as implemented in the ATLAS EM calorimeter

(like one Gy), saturates, and recovers afterwards. This loss was shown to be due to an increased absorption at short wavelengths (∼400 nm). Since 1 Gy is typical of the dose corresponding to one fill at high luminosity, a fast feedback follow-up of this effect is required. The choice made is to monitor the response using laser pulses sent to the front face of each crystal in sequence, during the empty cycles of the LHC. Comparing the losses on laser pulses to those observed with beam particles in the test area (see Figs. 34 and 35) it was shown that the ratio between the two is rather uniform (rms on 19 crystals is 6.3%), which will greatly simplify this follow-up [38].

The crystal to crystal normalisation will be known at start-up with an accuracy of 5%, from bench tests (^{60}Co source). This will be refined with LHC data using a combination of azimuthal uniformity, and E/p constraints. Large statistics of Z→ee decay will also place a useful constraint to reach the final goal of 0.5%. The calibration of several modules in beam (like 20%) will also be extremely useful. The absolute average normalisation of the calorimeter response will be made with reference to the Z^0 mass using Z→ee decays.

3.3.6 ATLAS EM calorimeter

For its EM calorimeter, barrel and end-caps, ATLAS has chosen a high granularity lead-liquid argon sampling technique with accordion geometry (Fig. 36).

The inner radius of the barrel active calorimeter part is 1.5 m, and the front faces of the two end-caps are located at $|Z|$=3.6 m. In order to correct for losses in dead material in front of the calorimeter (tracker, solenoid, cryostat), the calorimeter proper is preceded by a presampler layer. The barrel calorimeter is divided in two halves longitudinally; each half is built out of 16 modules. Similarly each end-cap wheel is assembled from 8 identical modules. Thanks to the accordion geometry the response is uniform in azimuth irrespective of module frontiers. The calorimeter

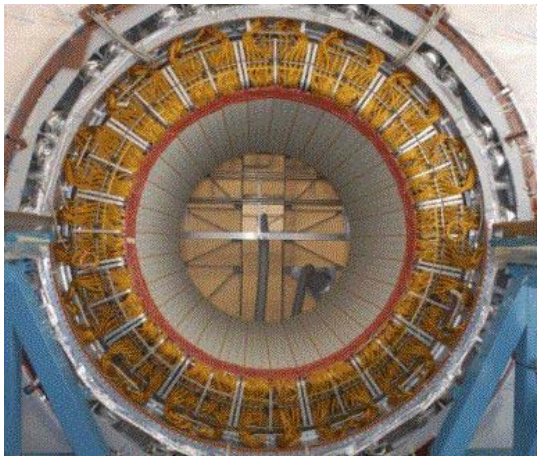

Fig. 37. The ATLAS EM barrel calorimeter (first half) in its cryostat

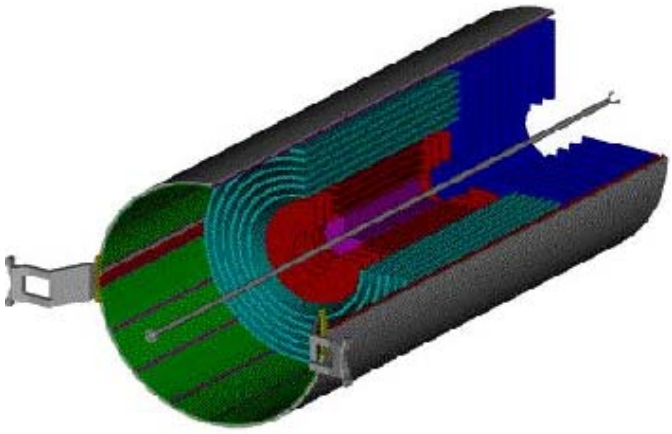

Fig. 39. Sketch of the CMS tracker layout

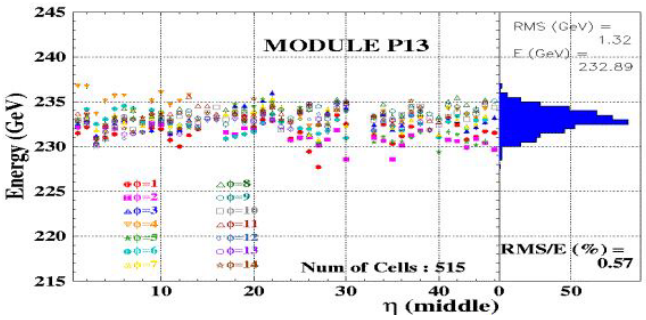

Fig. 38. Uniformity of response of a barrel ATLAS EM module, as observed in test beam

has 3 samplings in depth. The central layer has a granularity $\delta\eta$ x $\delta\phi$= .025 x .025. The first sampling has a very thin granularity in η (.003 x .1) in order to strengthen the photon-pizero (and thus the photon-jet) rejection; together with the middle sampling it provides photon pointing with an accuracy of 50 mr/$\sqrt{E}$. In total there are 175 000 electronics channels in the EM calorimeter with the front end part located on the cryostat. To cope with the high rate of the LHC, the preamplifiers and shaping amplifiers give a response to energy deposits which peaks after 40 ns and decays slightly slower. The electronics noise of a cell in the central sampling is about 30 MeV. The dynamic range of 16 bits is covered by 3 gains (in the ratio 1:10:100). Pipelining (analog) and digitisation are made on detector (most parts are realized in the radiation hard DMILL technology). Digital data is sent out by 1 GHz optical fibers upon LVL1 request at a maximum rate of 75 kHz. Summing in trigger towers of 0.1 x 0.1 is done in an analog way, on detector.

Figure 37 shows the first half-barrel integrated in the cryostat. The first end-cap is also assembled. Four barrel modules (out of 32) and 3 end-cap modules (out of 16) were thoroughly tested in beam at the CERN SPS. The qualification included a cell by cell scan in order to assess the uniformity of response. The result obtained for a barrel module [41] is shown in Fig. 38 . The rms of the distribution is 0.57%. In zones of 0.2 x 0.4 the uniformity is 0.4% or better. This uniformity is obtained from the electronics calibration system alone (correcting for a cell to cell variation of a small inductance inside the calorimeter, between the sensitive cell and the calibration element), and reflects the homogeneity of construction of the detector.

The strategy of ATLAS in view of reaching a constant term of 0.7% or better is to consider each zone of 0.2 x 0.4 as "uniform by construction and electronics calibration" and to check/correct for non-uniformities between zones using Z$\rightarrow e^+e^-$ decays. Given the rather limited number of such zones ($\sim$400) one day of data at 10^{33} should give enough Z^0 to meet the goal. No short-term variations of the response are expected. On the medium or long term side, temperature variation of the liquid bath (response drops by 2% for a temperature increase of 1 degree) or pollution of the liquid could impact the response. Care was taken to build the calorimeter with materials which do not outgas under irradiation.

The liquid argon calorimeter system of ATLAS (which also includes hadronic calorimetry from η=1.4 down to η=4.9) will be cooled down in a surface hall during year 2004, and then moved to the ATLAS pit.

3.3.7 The CMS tracker

The CMS tracker (see Fig. 39) is entirely based on Silicon sensors [42]. With a radius of 1.2 m and a length of 5.4 m it fills entirely the EM calorimeter inner cavity, and contains 210 m^2 of sensors. The detectors are arranged as a set of coaxial cylinders in the barrel part, and disks in the end cap part. A track going through all the detector sees typically 2 to 3 pixels layers and 10 to 14 strip layers. In total the detector has 10 million strips and 67 million pixels. Such a large volume, high granularity and high speed detector represents unfortunately a non-negligible amount of material in front of the calorimeter, inside the 4 T magnetic field. Typical figures are 0.4 X_0 at low η, and 1 X_0 or more from η=1 to end of acceptance (η=2.5).

An example of barrel strip module is shown in Fig. 40. The strips from two detectors (each about 9 cm long) are

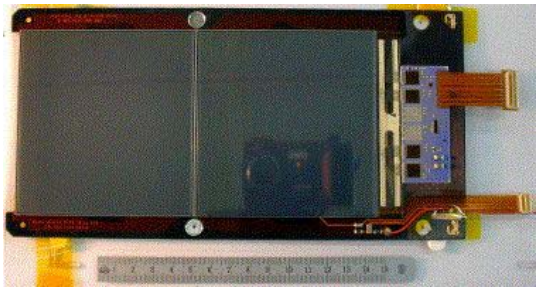

Fig. 40. A CMS barrel strip module

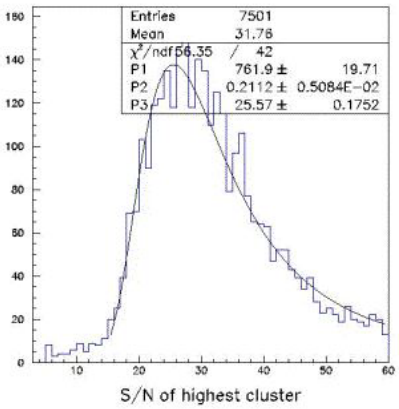

Fig. 41. Cosmic signal in a CMS strip detector

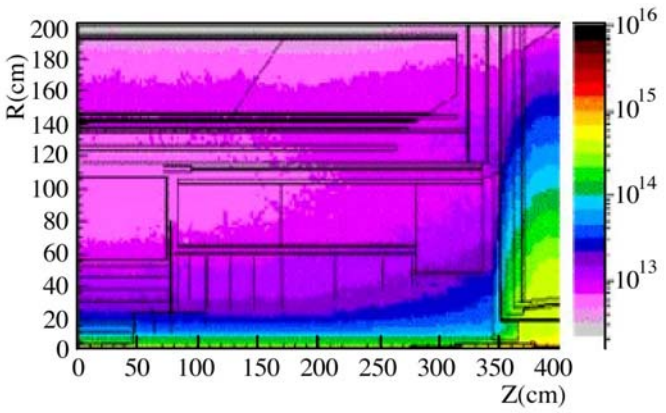

Fig. 42. Neutron fluence per high luminosity year in the ATLAS inner detector cavity

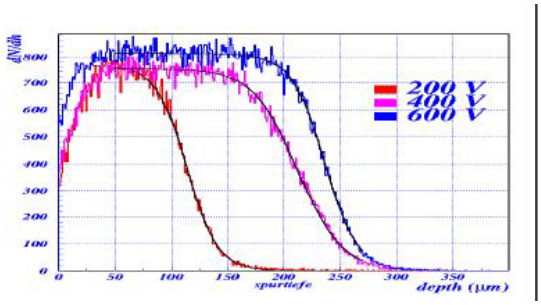

Fig. 43. Detector depletion from cluster size

connected by a bond wire, and then connected to the ASIC circuits, realized in DSM technology. An example of signal recorded with a series module (Fig. 41) shows the excellent signal to noise ratio.

The detector volume shall be kept at $-10°$ C, even during LHC shut-down, in order to prevent reverse annealing which would largely increase the leakage current across sensors, and thus the noise and the dissipated power. Sensor and electronics are currently being submitted to reception tests and assembled in modules like shown in Fig. 40.

3.3.8 The ATLAS pixel system

The ATLAS tracker system [43] is based on Si pixels in the innermost part, Si strips up to a radius of ∼55 cm, and is complemented at larger radius and larger z by a transition radiation straw detector(TRT), arranged as well in a barrel and disks (wheels) geometry.

The detector volume, and material in front of the LAr cryostat containing also the thin solenoid (field of 2 T) are similar to the CMS case. Some more details are given below, for illustration, on the pixel system, which consists of 3 cylinders with minimum radius of 4.3 cm and 2 x 3 disks. In order to cope with the most severe constraints posed on this system, namely the high level of radiations (Fig. 42 indicates a yearly neutron fluency of several 10^{13} n/cm^2), a "n on n oxygenated" sensor technology was chosen, together with DSM electronics connected to sensors by bump-bonding. In total the system has 82 million pixels of size 50 x 400 μm , with 2.8 % X_0 per layer.

The performance of different types of sensors under irradiation was tested in detail before choosing this technology (see also next section). Using beam particles at a ∼ 30 degrees incidence, it is possible to deduce the depletion depth from the cluster size. This is shown for series sensors in Fig. 43, which indicates full depletion at 600 Volts after 10^{15} n/cm^2, i.e. several years of LHC at full luminosity [44].

3.4 Tracking and vertexing beyond LHC

The future collider experiments (SLHC, Linear Colliders,VLHC) will share the trend towards higher luminosities, and the need to recognise displaced vertices in complex events. To meet such goals is going to require vertex detectors with higher granularity, less material per layer, less power dissipation and higher resistance to radiations than currently built devices.

The developments for linear colliders start from the route paved by CCDs, while developments in view of SLHC/VLHC are so far based on hybrid detectors, and go in the direction of defect engineering (an example is the use of oxygenated sensors for the ATLAS pixel system, oxygen atoms counter-balancing in some aspects p-type defects), or cold silicon, or diamond. Other initiatives like amorphous silicon on ASICs, depfets, 3-D silicon are also being pursued. The trend of electronics to go to smaller and smaller structure size (i.e. beyond 0.25μm)

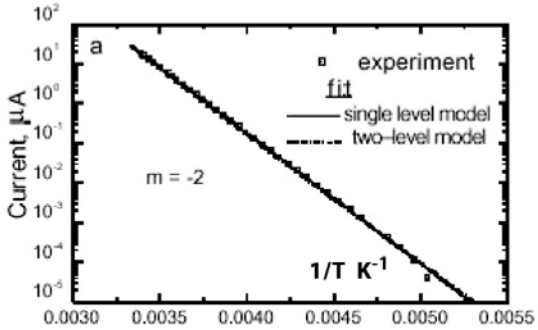

Fig. 44. Leakage current in silicon sensors as a function of inverse temperature (1/T)

may "naturally" solve the radiation hardness of electronics, although the associated low voltage range may not satisfy the dynamic range needed for very front-end elements.

3.4.1 Cold Silicon

Operation of silicon sensors at cryogenic temperatures ($\sim$ 100 K) brings several advantages for coping with high radiation levels (10^{15} n/cm^2 or more), but also some problems. Both are currently being studied by the RD39 collaboration [45]

- the leakage current, bulk and surface, goes down by huge factors (see Fig. 44),
- the carrier mobility is increased (it goes like $T^{-2.4}$) thus allowing faster response. This however may cause problems for operation in a strong magnetic field because of a too large Lorentz angle,
- CMOS electronics respond faster,
- heat conductivity of Silicon is increased, which ease cooling.

However charge trapping by deep defects may be more harmful than for room temperature operation, and needs to be compensated. Going in some more detail, it is known that levels created by irradiation are predominantly of p-type. Starting from a n-bulk detector, irradiation soon lead to type inversion, then the depletion voltage increases linearly with dose. The RD39 proposal is to adjust the net space charge by working in the forward bias mode with the necessary injected current. It was shown that staying in the very manageable range of 100 nA/cm^2 one can maintain a constant full depletion voltage up to several 10^{15} n/cm^2 equivalent. Some detectors engineered in this way will be used for tests in the COMPASS experiment at CERN.

3.4.2 Diamond detectors

Polycrystalline diamond detectors are grown since a few years in 5" wafer size by Chemical Vapor Deposition on Si-C base crystals [46]. Detailed studies undertaken in particular by the RD42 collaboration [46] have allowed to understand their properties as detectors for particle physics. The most important of them are summarised in Table 1.

Table 1. Comparative properties of diamond and silicon

	silicon	diamond
dE/dx(MeV/cm)	3.9	6
X_0 (cm)	9.4	12.5
ε_r	11.7	5.9
Band gap (eV)	1.14	5.5
$< E >$ /pair (eV)	3.6	13.1
Pairs/μm	110	36
Displacement threshold (eV)	13	43

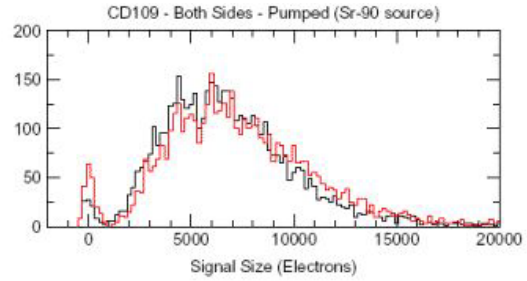

Fig. 45. Signal in polycrystalline diamond sensor

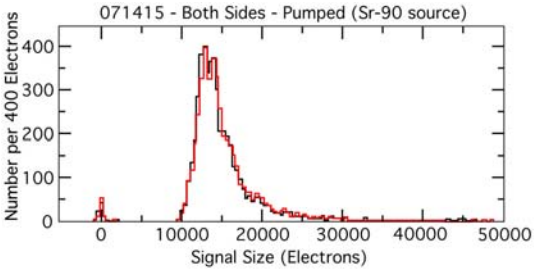

Fig. 46. Distribution of MIP signals in mono crystalline diamond sensor

Due to the growth process from a non-diamond base, the polycrystalline structure becomes more regular away from the interface. Given the large band gap, diamond behaves essentially like an insulator, and can be polarised either side. Due to defects between microcrystals a large electric field is necessary, in the absence of any irradiation, to fully collect the charge, typically 300 V for a 300 μm thick detector. Signals obtained in these conditions are wider than for silicon, again because of the microcrystalline structure. They are however, as shown in Fig. 45, sufficiently large to allow detection with a good efficiency. Irradiation tests have shown that the signals are barely affected up to the maximum tested of 2 x 10^{15}n/cm^2.

First examples of monocrystalline sensors, of maximum size 1cm^2 were recently made available. Exposed to beam particles they showed nice "Silicon like behaviour", as shown in Fig. 46 (signal shape). Their resistance to radiations will be soon explored [47].

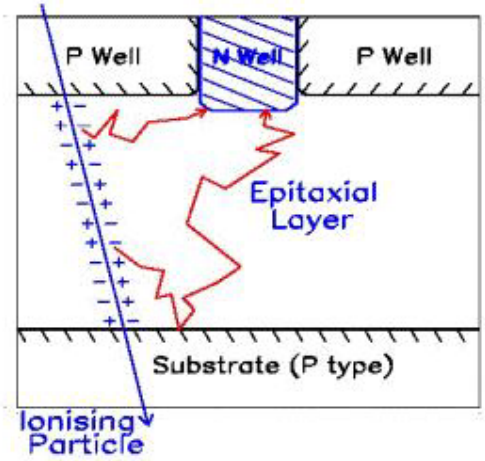

Fig. 47. Signal formation in CMOS active pixels

While progresses are regularly made, polycrystalline diamond sensors remain expensive, and can only be envisaged today for vertex detectors of ~ 1 m^2 or less. Mono crystalline diamonds are today reserved for development and very specific studies.

3.4.3 CMOS active pixels

As opposed to hybrid pixel detectors discussed above, in which electronic chips are bump-bonded to sensors, it is at first sight attractive to incorporate both functions on a single substrate, which in turn has to be able to support both of them. A successful example is CCDs, as used for example in the SLD vertex detector with the largest number of pixels ever operated (300 millions), but radiation soft and plagued by a slow sequential readout.

Another example currently under development "CMOS active pixels" [48], is also based on circuits for digital cameras. On a standard p-type substrate, of rather low resistivity, is grown an epitaxial layer. Structures for MOS transistors are then ion-implanted, and covered by an oxide layer. In such a structure the electrons from pairs created in the epitaxial layer move by thermal diffusion and reflexion on the p-type bulk and are collected by the n-well structure (see Fig. 47) in a few tens of ns. The behaviour of devices built in this way is governed by the smallness of all dimensions: the epitaxial layer is typically 10 μm thick, from which derives a rather small collected charge ($\sim$1000 electrons in total). In turn the pixels are also small (typically 20 x 20 microns) leading to a capacitance in the tens of fF range, and thus good signal to noise ratio ($\sim$30), even taking into account that the charge is split between several pixels ($\sim$10 or more).

Another interesting feature of these devices, like CCDs, is that all the "useful part" is localised at the surface of the wafer, allowing thinning down to 100 μm or even less. Besides radiation resistance, the critical aspect of the development is to implement a circuitry allowing fast readout with low power, while preserving the signal/noise ratio. A promising example currently being prototyped [48] is parallel processing of 128 pixels in a row, at 5 MHz. To each pixel (28 x 28 μm) is attached an amplifier and a 2 cell deep analog memory. In total the circuit has 29 transistors per pixel and dissipates 500 μW per column, ie 0.5 W/cm^2. While the readout speed (25 μs) would fit FLC requirements, the dissipated power is considered still too high, and will require further iterations. Devices of this type keep their properties (collected charge and noise) up to a fluence of 10^{11} to 10^{12}n/cm^2, and doses of up to 100 kRad. This may be enough to cope with the background at future linear colliders.

4 Summary and conclusions

The great variety of developments presented underlines the fact that there is no new major physics programme without an associated vigorous detector development.

Silicon detectors, now built in areas as large as 200 m^2 have revolutionized tracking at high rate. The large area strip detectors, and the high granularity pixel detectors for vertexing will still evolve in the direction of less material and higher speed while increasing their radiation resistance.

Precision EM calorimetry is dominated by crystals and noble liquids.

Both in tracking and calorimetry, Deep Submicron Asics rescued several rad-hard electronics projects.While the trend toward smaller structures will persist, it remains to be seen if the associated circuits will cover all high energy physics needs, in particular the dynamic range of the very front ends.

Cryogenic technologies remain essential, and even increase their range of application. This goes from "Liquid nitrogen cryogenics" for calorimetry, to "liquid helium" technology for super conducting magnets, and to the ^{3}He/^{4}He dilution systems for bolometers in the 100 mK range.

First data from the LHC, in 4 years, will be the final validation for the wealth of developments embedded in ALICE, ATLAS, CMS, and LHCb.

Meanwhile, the R&D for detectors at Future Linear Colliders should get completed.

Acknowledgements. My warm thanks go to all colleagues who kindly supplied information about their detectors, or who helped me in understanding some of their subtleties.

Preparing this written summary would not have been possible without the efficient help of C. Drouet and her colleagues of the LAL scientific secretary's office.

References

1. TPC in Heavy Ion experiments. J. Lien, talk presented at this Conference
2. Development of a TPC for the Future Linear Collider. S. Roth, talk presented at this Conference
3. Precision chambers for the ATLAS experiment. S. Mohrdiek, talk presented at this Conference. The CMS

Muon Detector. M. Cerrada, talk presented at this Conference
4. RPCs in running and future experiments. G.L. Bruno, talk presented at this Conference
5. See for example: M.A. Bizouard, status of Virgo, talk presented at Moriond, March 2003
6. see for example: LIGO and GEO developments for Advanced LIGO, S. Rowan, APS meeting, April 2003
7. P.R. Roach and B.P.M. Helvensteijn: Proc. of the 6th Int. Cryocooler Conference. Plymouth MA (1990)
8. P.L. Richards: J. Appl. Phys. **76**(1), (1994)
9. P.D. Mauskopf et al.: Applied Optics, **36**, N°4 (1997)
10. W.C. Jones et al.: astro-ph/0209132, Sept 2002
11. http://astro.estce.esa.ul/astrogen/planck/
12. N.J.T. Smith et al.: Proc. of the 4th Int workshop on Identification of dark matter (World Scientific, Singapore 2002)
13. X.F. Navick et al.: Nucl. Instrum. Methods A **444**, 361 (2000). A. Broniatowski et al.: Nucl. Instrum. Methods A **444**, 327 (2000)
14. D. Abrams et al.: Phys. Rev. D **66**, 122003 (2002)
15. M. Bravin et al.: Astropart. Phys **12**, 107 (1999); S. Cebrian et al.: Nucl. Phys. Proc. Suppl. **110**, 97 (2002)
16. P. Nolan et al.: IEEE Trans. Nucl. Sci. **NS-39**, 993 (1992)
17. E. Bloom et al.: SLAC-R-22 Feb 1998. See also L. Latronico: Nucl. Instrum. Methods A **511**, 68 (2003)
18. E. do Couto e Silva et al.: SLAC-PUB-8682 (2000)
19. E. Andres et al.: Nature **410**, 441 (2001)
20. E. Aslanides et al.: astro-ph/9907432
21. Nestor: see for example A. Tsirigotis, talk presented at this Conference
22. See for example: J. Rico, talk presented at this Conference
23. M.L. Brooks et al.: Phys. Rev. Lett. **83**, 1521 (1999)
24. J. Hisano, D. Nomura, T. Yanagida: Phys. Lett. B **437** 351 (1998)
25. R. Barbieri, L.J. Hall: Phys. Lett. B **338**, 212 (1994)
26. T. Mori et al.: Research proposal for experiment at PSI (1999)
27. T. Doke, K. Masuda, E. Shibamura: Nucl. Instrum. Methods A **291**, 617 (1990)
28. See for example: S. Mihara, talk given at "9th Pisa Meeting on Advanced Detectors" La Biodola, Isola d'Elba (May 2003)
29. STAR-Rich: see for example A. Braem et al.: Nucl. Instrum. Methods A **449** 720 (2003). Alice Collaboration: TDR for High momentum particle identification detector CERN/LHCC 98-19
30. CDF II Technical Design report Fermilab-Pub-96/390-E
31. See for example: W. Ashmanskas, talk presented at "9th Pisa Meeting on Advanced Detectors" La Biodola, Isola d'Elba (May 2003)
32. The CMS Solenoid TDR CERN/LHCC 97-10
33. The ATLAS Barrel Toroid TDR CERN/LHCC 97-19
34. The Alignment system for the Atlas muon spectrometer: C. Amelung: talk presented at this Conference
35. The CMS hadronic calorimeter TDR CERN/LHCC 97-31
36. J. Freeman: talk given at "9th Pisa Meeting on Advanced Detectors" La Biodola, Isola d'Elba (May 2003)
37. The CMS Electromagnetic calorimeter TDR CERN/LHCC 97-33
38. See for example F. Cavallari, R. Rusak, E. Auffray: talks given at CALOR 2002 (World Scientific R.Y Zhu editor)
39. The ATLAS Liquid argon calorimeter TDR CERN/LHCC 96-41
40. The ATLAS calorimeter Performance TDR CERN/LHCC 96-40
41. B. Aubert et al.: Nucl. Instrum. Methods A **500**, 178 (2003); B. Aubert et al.: Nucl. Instrum. Methods A **500**, 202 (2003). See also L. Di Ciaccio: talk presented at this Conference
42. The CMS Inner detector TDR CERN/LHCC 98-6
43. The ATLAS Inner Detector TDR CERN/LHCC 97-16 and 97-17
44. A study of charge trapping in irradiated silicon with test beam data. G. Alimonti et al.: ATLAS note INDET-2003-014
45. See for example: K. Borer et al.: RD-39 status report CERN/LHCC 2002-004
46. See for example: W. Adam et al.: RD-42 status report CERN/LHCC 2002-010
47. Recent Developments in Diamond detectors. A. Oh, talk presented at this Conference
48. Y. Gornushkin et al.: Nucl. Instrum. Methods A **478**, 311 (2002); W. Dulinski, talk given at "9th Pisa Meeting on Advanced Detectors" La Biodola, Isola d'Elba (May 2003)